Microvascular Ion Transport through Endothelial Glycocalyx Layer: New Mechanism and Improved Starling Principle

Xi Zhuo Jiang (XZJ), Yiannis Ventikos[*] (YV), Kai H. Luo[*] (KHL)

Department of Mechanical Engineering, University College London, Torrington Place, London WC1E 7JE, UK

***Corresponding Author:**

YV: y.ventikos@ucl.ac.uk

KHL: k.luo@ucl.ac.uk

Postal Address: Department of Mechanical Engineering, University College London, Torrington Place, London WC1E 7JE, UK

Tel: +44 (0)20 7679 3916

Author Contribution:

XZJ conducted the simulation, analyzed the results, and drafted the manuscript.
YV finalized the manuscript and supervised the research.
KHL finalized the manuscript and supervised the research.

Running Head: Microvascular ion transport through EGL

Downloaded from www.physiology.org/journal/ajpheart at UCL Library Services (144.082.114.165) on May 14, 2019.

Abstract: Ion transport through the endothelial glycocalyx layer is closely associated with many vascular diseases. Clarification of ion behaviors around the endothelial glycocalyx layer under varying circumstances will benefit pathologies related to cardiovascular and renal diseases. In this research, a series of large-scale molecular dynamics simulations are conducted to study the response of ion transport to the changing blood flow velocity and the shedding of endothelial glycocalyx sugar chains. Results indicate that blood flow promotes the outward Na^+ transport from the near-membrane region to the lumen via the endothelial glycocalyx layer. Scrutiny of sugar chain dynamics and their interactions with Na^+ suggests that corner conformation of endothelial glycocalyx sugar chains confines the movement of the Na^+ whereas stretching conformation facilitates the motion of Na^+ ions. The flow impact on ion transport of Na^+ is non-linear. Based on the findings, the Starling principle and its revised version, which are prevailingly used to predict the ion transport of the endothelial glycocalyx layer, are further improved. An estimation based on the further revised Starling principle indicates that physiological flow changes the osmotic part of transendothelial water flux by 8% compared with the stationary situation.

Keywords: ion transport; endothelial glycocalyx layer; Starling principle; microvascular

New and Noteworthy:

The biophysical roles of negatively charged oligosaccharides of the endothelial glycocalyx have gained increasing attention due to their importance in regulating microvascular fluid exchange. The Starling principle and its revisions are at the heart of the understanding of fluid homeostasis in the periphery. Here, the blood flow changes the conformations of glycocalyx sugar chains, thereby influencing

Downloaded from www.physiology.org/journal/ajpheart at UCL Library Services (144.082.114.165) on May 14, 2019.

availability of Na^+ for transport. Based on the findings, the Starling principle and its revision are further improved.

Downloaded from www.physiology.org/journal/ajpheart at UCL Library Services (144.082.114.165) on May 14, 2019.

Introduction

Endothelial glycocalyx layer (EGL) is a thin layer with a thickness of 50 to 500 nm coating endothelial cells. The EGL features the dendritic structures of the endothelial glycocalyx (EG) which has been extensively studied for its functionality as a mechanotransducer (43, 44). Meanwhile, the EGL is also recognized as an effective Na^+ buffer (30) due to the negatively charged sugar chains of the glycocalyx (32, 38, 47). Vascular diseases are intimately associated with the extracellular ion concentrations (20, 29). For example, *ex vivo* results indicate that sodium overload could stiffen the vascular endothelial cells (31) and alter the release nitric oxide which is a hallmark of endothelial function (20).. In previous studies, the impact of salt on the endothelial and vascular phenotype has been clarified (20); however, its inverse problem — how the endothelial surface structure (i.e. EG) affects the ion behavior — has not been sufficiently studied. Furthermore, as endothelial cells are the first barrier directly exposed to blood, what is the consequence of a changing blood velocity on ion distributions? The answers to these problems will contribute to our understanding of pathologies of EG-related renal and cardiovascular diseases.

The mechanism describing fluid transport in EGL is the Starling principle (41). According to this principle, the movement of flow across semipermeable membranes is determined by the net imbalance between the hydraulic pressure difference and the osmotic absorption pressure of the plasma proteins. Since the net imbalance drives the motion of solutes, it is also called the filtration force (FF) in the Starling principle. When the Starling principle is applied to EGL, the osmotic pressure difference has to be revised by considering the colloid osmotic pressure beneath the EGL (21). In the revised Starling principle, the FF is calculated by:

Downloaded from www.physiology.org/journal/ajpheart at UCL Library Services (144.082.114.165) on May 14, 2019.

$$\mathrm{FF} = \Delta P - \sigma(\Pi_p - \Pi_g) \tag{1a}$$

In Eq. (1a), ΔP is the hydrostatic pressure difference, σ is the Staverman's osmotic reflection coefficient (42) representing the degree of leakiness to a specific solute, and ranges in value from 0 to 1. Π_p and Π_g are the osmotic pressure in plasma and beneath the EGL, respectively.

Incorporating Jacobus van't Hoff's law relating osmotic pressure to solute concentration, (i.e. $\Pi = iRTc$), the FF can be rewritten as

$$\mathrm{FF} = \Delta P - \sigma iRT(c_p - c_g) \tag{1b}$$

where i is the dimensionless van't Hoff index, R is the ideal gas constant and T is the temperature, c_p and c_g are the molarities in plasma and beneath the EGL, respectively.

Despite the successful applications of the revised Staring principle to predicting fluid exchange as reviewed by Levick and Michel (21), the principle seems to be unable to answer our proposed question – will changes in blood velocity affect ion distributions? If at all, what is the mechanism for such an influence? Meanwhile, we are also curious about the influence of the EG structure and composition on fluid exchange, which is also an open question attracting intense interest from scientists.

In this context, the objective of this research is to investigate the response of the endothelial ion distribution (mainly Na^+) to the modification of two principal factors associated with cardiovascular diseases (i.e. change of blood velocity (44) and shedding of EG sugar chains (5)). To mimic the two scenarios, large-scale molecular dynamics (MD) simulations with fine structural information of the EG biomolecules and surrounding ions are conducted. Dynamics of the biomolecules and the surrounding ions (e.g. Na^+) are to be scrutinized. Finally, a further revision of the

Downloaded from www.physiology.org/journal/ajpheart at UCL Library Services (144.082.114.165) on May 14, 2019.

Starling principle considering changing blood flow velocity and EG configuration is proposed.

Methods

System construction. Three EG elements, each of which is composed of a core protein and six sugar chains, are considered in this research. Syndecan-4 (Syn-4) proteoglycan and heparin sulphate (HS) sugar residues are selected to model the EG core protein and sugar chains, respectively. As shown in Fig. 1a, the whole space is divided into two compartments by the lipid bilayer. Above the lipid bilayer is the ectodomain, representing the space outside the endothelial cells, where flow passes by. This region contains negatively-charged HS sugar chains, Syn-4 ectodomain in connection with HS sugar chains, water molecules and ions. Below the lipid bilayer is the cytoplasm, representing the inner space of the cell, which is filled with the Syn-4 cytoplasmic protein, water molecules and ions. All the biomolecules are solvated and ionized to NaCl solution with a concentration of 0.1 M NaCl. Together with the Na^+ added to neutralize the negatively charged EG elements, the total Na^+ molarity in the intact EG cases (i.e. Cases a to d in Table 1) is about 0.15 M, and Cl^- molarity is 0.1 M. The simulation box is a hexagonal prism with an area of 820 nm^2 and height of 72 nm. The flow/EG system comprises 5,800,000 atoms in total.

Protocol details. The TIP3P water model (18) was selected to simulate water molecules. The CHARMM biomolecular force field (23) was applied on proteins and the lipid bilayer. Force field parameters for sugar chains have been validated in previous studies (6).

The system was first equilibrated under an isothermal-isobaric ensemble, followed by a canonical ensemble. The velocity Verlet integration method (2) was

Downloaded from www.physiology.org/journal/ajpheart at UCL Library Services (144.082.114.165) on May 14, 2019.

used to advance the positions and velocities of atoms in time steps of 2-fs. Particle mesh Ewald (8) electrostatics with a grid density of $1/Å^3$ was used. The SETTLE algorithm (28) was used to enable the rigid bonds connected to all hydrogen atoms. The van der Waals interactions were calculated using a cut-off of 12 Å with a switching function starting at 10 Å (6). The last frame of the equilibrium simulation was used as the initial configuration of every simulation involved in this research as listed in Table 1. In flow simulations, a Lowe-Andersen thermostat, a specific thermostat exclusively for flow problems, was selected to maintain the temperature at 310K. Periodic boundary conditions were used in all three directions. Detailed set-up about the boundary conditions was introduced in our previous publications (14, 16).

All MD simulations were performed using the software suite NAMD 2.9(34). The visualization of the molecular structures was performed via the VMD (12) package. All parallel simulations and non-visualized post-processing were conducted on ARCHER, UK's national supercomputing service. To obtain a simulation result with physical time of 1 ns, 9,000 compute cores were simultaneously used for about 2 hours.

Details about the construction of the flow/EG system and the protocol information can be found in our previous publication (16).

Flow simulations and case set-ups. In this research, NaCl solution was used as a simplification of the blood flow, as the focus of this study was the ion transport through the EGL. To generate a flow in the ectodomain, external forces in the *x* direction were imposed on oxygen atoms of water molecules in the ectodomain, and the tactic has been practiced in previous MD studies (14, 16, 35). As reported in our previous study (16), an external force with an order of magnitude of 0.001 fN would

Downloaded from www.physiology.org/journal/ajpheart at UCL Library Services (144.082.114.165) on May 14, 2019.

142 generate a laminar flow with a physiological bulk flow velocity; the presence of the
143 EG disturbs the flow profiles, leading to the oscillations of velocity distribution in
144 space. For the bulk flow, according to Newton's Law of Motion and assuming the
145 changes in interactions between water molecules and surroundings can be neglected,
146 the resulting bulk flow velocity is supposed to be in proportion to the external force.
147 Thus, the cases with changing blood flow velocity were simulated via changing the
148 strengths of external forces. To study the Na^+ behavior under various EG
149 configurations, two shedding scenarios of the sugar chains were also constructed.
150 Meanwhile, a diffusion case in which no external forces were imposed on water
151 oxygens was also studied. Table 1 summarizes principal parameters of the *in silico*
152 experiments involved in this research.

153 **Table 1 Principal parameters for *in silico* experiments.**

Case	External force, f (fN)	Number of sugar chains, N	Physical time (ns)
a	0.003	18	30
b	0.002	18	21
c	0.001	18	21
d	0	18	8
e	0.003	15	15
f	0.003	9	15

154

155 **Stratifying the ectodomain.** To explore the spatial distribution of charges, a
156 space with a height of 50 nm in the ectodomain was stratified into 25 equal bins (14).
157 In each bin, the molarities of sugar chains and ions (Na^+ and Cl^-) were calculated.

Downloaded from www.physiology.org/journal/ajpheart at UCL Library Services (144.082.114.165) on May 14, 2019.

158 **Statistical analysis.** Differences of means were analyzed by ANOVA for every
159 two groups. In Fig. 2a, the base case is Case d (with an external force of 0), and
160 sample sizes of Cases a to d are 300, 210, 210, and 80, respectively. In Fig. 2b, the
161 base case is Case a (N=18), and the first 150 samples are used herein. Sample sizes of
162 both Cases e (N=15) and f (N=9) are 150. In Fig. 5a, the base case is Case d (with an
163 external force of 0), and sample sizes of Cases a to d are 300, 210, 210, and 80,
164 respectively.

165 **Results**

166 **Distribution of Na^+ molarity around the EGL**

167 To investigate the Na^+ transport through the EGL, the spatial distribution of ions
168 is a prerequisite. The EG features its negatively charged sugar chains in the
169 ectodomain, and the charge distribution of the sugar chain residues in terms of
170 molarity is illustrated in Fig. 1b. The molarity distribution used in this research is
171 consistent with previous experimental results in order of magnitude (1, 11, 13). To
172 maintain a neutral system, in the region with rich sugar chains (below 42 nm in
173 height), the initial Na^+ molarity distribution along height (Fig. 1c) is nearly symmetric
174 to its sugar residue counterpart (17). Fig. 1c also indicates that the Na^+ molarity near
175 the lipid membrane region (e.g. h = 6 nm) prevails over that (c_p) above the sugar chain
176 rich region (e.g. h = 46 nm) (17). The pertinent Na^+ molarities in individual regions
177 are c_g and c_p in Eq. (6). For simplification, the Na^+ molarities at h = 6 nm and h = 46
178 nm were used to estimate c_g and c_p, respectively.

179

180 Fig. 2a illustrates the Na^+ molarity differences ($\Delta c = c_g - c_p$) in the two regions
181 beneath and above the sugar chain rich area with normalized time (defined as the ratio

Downloaded from www.physiology.org/journal/ajpheart at UCL Library Services (144.082.114.165) on May 14, 2019.

of instantaneous time over the total time involved) under changing flow velocities via varying the values of external forces. The mean molarity difference value of the time series in the equilibrium (no flow) case is greater than its flow counterparts (p(0.003fN, no flow) < 0.005 and p(0.002fN, no flow) < 0.005). This phenomenon indicates that the flow facilitates the diffusion of Na^+ across the dendritic sugar chain area, and the facilitation is consistent with the convection-diffusion transport phenomenon at macroscales (33).

The scenarios of sugar chain shedding are accomplished via reducing the number of sugar chains (The removal strategy is described in detail in Ref. (15).). Due to the removal of the negatively charged sugar chains, the initial Na^+ distribution has been modified to maintain a neutral system. To facilitate comparison, a relative molarity difference is adopted to study the effects of sugar chain numbers on the ion transport. The relative molarity difference, $\underline{c}$, is defined as in Eq. (2).

$$\underline{c} = \frac{\Delta c - \Delta c_0}{\Delta c_0} = \frac{\Delta c}{\Delta c_0} - 1 \tag{2}$$

where Δc is the molarity difference as defined previously, and Δc_0 is the molarity difference at the start of every simulation. Fig. 2b illustrates the relative molarity differences under situations with various numbers of sugar chains. The Na^+ molarity gradient orients from the lipid membrane to the flow regardless of whether the sugar chains are partially removed or not, for the value of relative molarity difference is greater than -1 for all the three situations. Furthermore, dramatic decreases in the molarity differences are also observed in the sugar chain reduced cases (Cases e and f in Table 1), as negative values of $\underline{c}$ are frequently observed during the time series as shown in Fig. 2c. In Cases e and f, the removal of the sugar chains reduces the steric hindrance for outward Na^+ ion transport, resulting in the decrease in the molarity

Downloaded from www.physiology.org/journal/ajpheart at UCL Library Services (144.082.114.165) on May 14, 2019.

206 difference Δc. Therefore, the negativity of $\underline{c}$ values in these two cases implies an
207 impairment in the functionality of the EG as a filter or buffer for Na^+ ions.

208 **Mechanism for flow impact on Na^+ transport**

209 Fig. 2a shows that the blood flow velocity affects the Na^+ ion transport. In Fig.
210 2b, the influence on transport from the geometric configuration of sugar chains can
211 also be partially attributed to the velocity change due to the reduction of sugar chains.
212 Therefore, to reveal the mechanism of flow impact on Na^+ ion transport is to find out
213 the pathway via which flow affects the Na^+ behavior.

214 **Conformations and interactions**. Previous computational (14, 35) and
215 experimental (40) studies suggest that flow modifies conformations of biomolecules
216 (e.g. sugar chains). To elucidate whether the conformational changes influence Na^+
217 behavior, two sugar chains of the same composition with different initial
218 conformations (Fig. 3a) are selected from the no-flow case (Case d in Table 1) and
219 their interactions in terms of the coordination numbers (CNs) of surrounding Na^+ ions
220 are examined. The CNs of the surrounding Na^+ ions are quantified by the numbers of
221 heavy atoms (i.e. nitrogen, oxygen and sulphate atoms) of the sugar chain residues
222 within a cut-off distance of 2.5 Å around the Na^+ ions (The value of the cut-off
223 distance is based on the radial distribution result reported in Ref. (9)). Time-
224 evolutions of the average CNs of Na^+ are illustrated in Fig. 3b, together with the
225 probability density distributions in Fig. 3c. The conformations of sugar chains are
226 measured via a center-to-center vector ($\boldsymbol{R}_{\mathbf{ctc}}$) connecting the two centers of mass of a
227 bisected sugar chain, which is reported effective in describing polymer rotational
228 dynamics (19). Three geometric parameters related to the vector $\boldsymbol{R}_{\mathbf{ctc}}$, as illustrated in
229 Fig. 3d, are used to depict the conformations of the two sugar chains with their time-

Downloaded from www.physiology.org/journal/ajpheart at UCL Library Services (144.082.114.165) on May 14, 2019.

evolutions shown in Fig. 3e to 3g. As illustrated in Fig. 3e to 3g, the conformations of the two sugar chains vary in dissimilar patterns. Thus, it can be concluded that the sugar chain conformations affect the interactions between the Na^+ ions and sugar chains.

The major conformational difference of the two sugar chains of interest (Fig. 3a) resides in segments with corner shapes. To reveal how the corner shape affects the interaction between Na^+ and sugar chains, two segments with identical residue sequence but one featuring a corner shape and the other with a stretching shape are selected as labelled in the inner panel of Fig. 4a. The numbers of Na^+ around both segments throughout the no-flow simulation are recorded. The probability density distributions of the surrounding Na^+ numbers in Fig. 4a suggest that the corner conformation of the sugar chain favors the accumulation of Na^+; by contrast, its stretching counterpart facilitates the movement of the Na^+. To further explore how the corner conformation accumulates Na^+, the residence rates of initial Na^+ ions around the corner and stretching conformations are calculated. The residence rate is calculated as

$$\text{residence rate} = \frac{n_{Na,j}}{n_{Na,0}} \tag{3}$$

In Eq. (3), $n_{Na,j}$ is the number of Na^+ ions retained from the initial frame of the simulation at the instant j, and $n_{Na,0}$ is the number of Na^+ ions at the initial frame of the simulation. As shown in Fig. 4b, the higher residence rate of Na^+ in the corner case indicates that more ions stay around the corner sugar chain. At the initial stage, B01B chain has a corner conformation which traps the ions, resulting in a high residence rate. As the corner conformation gradually uncoils, the trapped ions are

Downloaded from www.physiology.org/journal/ajpheart at UCL Library Services (144.082.114.165) on May 14, 2019.

253 released, leading to a comparable residence rate to the A01B chain. Therefore, the
254 corner conformation accumulates Na^+ by confining the ions within its "realm".

255 **Flow and Na^+/sugar-chain interactions.** As reported in our previous MD
256 research (16) and an experimental study (40), flow can stretch coils of sugar chains.
257 Consequently, fewer corner structures are expected in flow cases. To further quantify
258 the corner structures, an index— solvent accessible surface area (SASA) (24) — is
259 calculated in individual cases. SASA is the area of the surface swept out by the center
260 of a probe sphere rolling over a molecule. For the union of atom balls, SASA is the
261 boundary of the ball union to have their radius increased by the probe radius (usually
262 1.4 Å as used in this research). The total SASAs of all sugar chains in the NaCl
263 solution were calculated and averaged by the total residues therein. A larger value of
264 average SASA per residue implies fewer corner structures within the sugar chains. As
265 illustrated in Fig. 5a, comparison of the average SASA values among the flow and the
266 no-flow cases suggests a decreasing number of corners when flow passes by, as
267 expected. Accordingly, fewer ions in the sugar-chain-rich region are observed in flow
268 cases. In other words, more Na^+ ions are carried out of the sugar-chain-rich region in
269 the flow cases, which explains the smaller concentration differences of the flow cases
270 (Fig. 2a) from the perspective of the geometry. In Fig. 5a, the SASA values increase
271 when flow passes by, but do not increase as the external force increases. The increases
272 in SASA values in the flow cases can be attributed to the disturbance of the
273 equilibrium of the sugar chains from the external force: the flow activates the motion
274 of sugar chains away from the equilibrated states. Nevertheless, the external forces
275 applied here are not strong enough to cause severe deformations of the sugar chains
276 (14), which lends the flow to an obstacle-dominant regime as discussed in Ref. (15),

Downloaded from www.physiology.org/journal/ajpheart at UCL Library Services (144.082.114.165) on May 14, 2019.

277 leaving the unpredictable relationship between the SASA values and the external
278 forces.

279 Flow causes conformational changes of sugar chains thereby affecting the
280 Na^+/sugar-chain interactions; on the other hand, it also breaks the equilibrium
281 between Na^+ ions and sugar chains via transferring momentum to ions. Fig. 5b
282 displays two snapshots of the sugar chain conformations and velocity fields of the
283 surrounding Na^+ ions in a fixed region of the simulation domain of Case a. As
284 illustrated in Fig. 5b, flow modifies the velocity fields of ions as it changes the
285 conformations of sugar chains. As flow accelerates, the average SASA decreases (Fig.
286 5a) which benefits the residence of Na^+ ions in the sugar-chain-rich region; however,
287 the large impulse from water molecules on Na^+ can also facilitate the movement of
288 ions thereby promoting the ion transport. Therefore, the impact of flow velocity on
289 ion transport is non-linear. A rough estimation shows that the order of magnitude of
290 Na^+ hydration energy (~100 kcal/mol (27)) is 100 times larger than the electrostatic
291 interactions between Na^+ and sugar chains (~ kcal/mol (25)). Thus, when flow
292 accelerates, the impulse from water molecules dominates the ionic movements: water
293 molecules collide and transfer momentum to ions, which encourages the *z*-direction
294 motion of Na^+ thereby promoting the Na^+ transport. Particularly, a negative
295 correlation between the Na^+ molarity difference and flow velocity can be expected.

296 Indeed, the large impulse case (Case a) also geometrically primes the Na^+
297 transport. A scrutiny of three components of the vector $\boldsymbol{R}_{\mathbf{ctc}}$ indicates that a large θ
298 value is observed in the 0.003fN case (Fig. 5c), and the large θ value can
299 geometrically facilitate the ion transport out of the sugar-chain-region. Consequently,
300 a declining number of Na^+ ions are observed in the sugar-chain-region as the external
301 force increases (Fig. 5d).

Downloaded from www.physiology.org/journal/ajpheart at UCL Library Services (144.082.114.165) on May 14, 2019.

302 **Further revision of Starling principle**

303 Considering the gradient of Na^+ ions around the EGL and the influence of flow
304 velocities and sugar chain configurations, the filtration force in the revised Starling
305 principle for Na^+ ions is proposed to be in the form

306 $$\mathrm{FF} = \Delta P + \sigma(\Pi_{\mathrm{g}} - \Pi_{\mathrm{p}})\gamma = \Delta P + \sigma iRT(c_{\mathrm{g}} - c_{\mathrm{p}})\gamma \quad (4)$$

307 In Eq. (4), γ is the revising coefficient for including the effects of flow velocity
308 and sugar chain configuration, and is expected to be determined by

309 $$\gamma = \frac{\Delta c\left(\bar{v}_x, \rho_N\right)}{\Delta c\left(\bar{v}_x = 0, \rho_{N,\mathrm{intact}}\right)} \quad (5)$$

310 In Eq. (5), $\overline{v}_x$ is the bulk flow velocity, and ρ_{N} is the geometric density of sugar
311 chains. For example, in this research, ρ_{N} is the ratio of the number of sugar chains to
312 the area of lipid bilayer patch. In the equation, the numerator is the molarity
313 difference under a certain flow velocity and a certain sugar chain configuration; the
314 denominator is the molarity difference in equilibrium system with intact sugar chains.

315 To determine γ, the relation between the molarity difference and the blood flow
316 velocity together with the geometric density of sugar chains needs to be established.
317 Although the previous section suggests a complicated effect of flow velocity on the
318 Na^+/sugar-chain interactions, for simplification, linear relation is still assumed here.
319 Indeed, raw data of Table 2 implies that linear relation is capable of describing the
320 trend of the changing molarity differences with flow velocity and geometric density of
321 sugar chains. Therefore, the molarity difference is expressed as:

322 $$\Delta c\left(\bar{v}_x, \rho_N\right) = a_0 + a_1\bar{v}_x + a_2\rho_N \quad (6)$$

Downloaded from www.physiology.org/journal/ajpheart at UCL Library Services (144.082.114.165) on May 14, 2019.

In Eq. (6), a_0 is the intercept of the linear regression, and a_1 and a_2 are the coefficients for velocity and geometric configuration of sugar chains, respectively. For demonstration, the intercept and coefficients are calculated based on the raw data (provided in Table 2 with Δc_a representing the average molarity difference throughout an individual time-evolution) of the cases in Table 1. In linear regression of multiple variables, the intercept and coefficients are $a_0 = 0.0336$, $a_1 = -0.1091$ and $a_2 = 1.6802$. Incorporating these values into Eq. (5) and also assuming that ρ_N being 18/820 nm^{-2} in this research is the normal physiological situation without shedding of sugar chains then gives

$$\gamma = \frac{0.0336 - 0.1091\bar{v}_x + 1.6802\rho_N}{0.0705} \tag{7}$$

Table 2 Raw data of cases listed in Table 1

Case	Δc_a (M)	v_x (m s^{-1})	ρ_N (nm^2)
a	0.062	0.0556	18/820
b	0.065	0.0953	18/820
c	0.067	0.0153	18/820
d	0.071	-0.0035	18/820
e	0.026	0.3411	15/820
f	0.028	0.2240	9/820

As a rough estimation, the coefficient γ in Case a is 0.92, which means physiological flow changes the osmotic part of transendothelial water flux by 8% compared with a stationary situation.

It is noteworthy that Eq. (1b) is valid for dilute solution, and the derivation of the improved Starling principle in this research is based on Eq. (1b). Thus, the coefficients proposed by this research are valid for dilute solution.

Downloaded from www.physiology.org/journal/ajpheart at UCL Library Services (144.082.114.165) on May 14, 2019.

Discussion

Osmotic reflection coefficient

The value of σ of capillary walls to NaCl in single perfused capillaries of the frog mesentery was experimentally determined to be 0.068 ± 0.03 by Curry *et al*. (7) before the indication of the EG as a semipermeable layer. In the following discussion, we would refer the value to individual ions (i.e. Na^+ and Cl^-), as Na^+ and Cl^- ions are distributed differently around the EGL. We shall discuss the likely value change based on the present results.

In their experiment, σ is estimated in accordance with the classic Starling principle where $FF=\Delta P - \sigma iRT(c_p - c_i)$; c_i is the solute concentration on the interstitial fluid side and approaches zero in the experiment. FF and ΔP were first determined or measured, before σ was calculated by the expression $\sigma = (\Delta P - FF)/[iRT(c_p - c_i)]$. We first discuss how σ is changed by the evaluation from the revised Starling principle. Indeed, discrepancy would occur if σ is calculated by the revised Starling principle (Eq.(1b)) where $\sigma = (\Delta P - FF)/[iRT(c_p - c_g)]$. To distinguish, σ_{cl} refers to the value obtained from the classic Starling principle and σ_{re} for its revised counterpart. Give that c_g may affect the orientation of osmotic pressure gradient, it is convenient to use the absolute values to calculate σ, i.e. $\sigma_{cl} = |\Delta P - FF|/(iRT|c_p - c_i|)$ and $\sigma_{re} = |\Delta P - FF|/(iRT|c_p - c_g|)$. The molarity of Na^+ added in the experiment is 0.1 M (total 0.21 M, including Na^+ from original perfusate) (7), which means $|c_p - c_i| = 0.1$ M (c_i is assumed to be 0 in the classic Starling principle). In our simulation, as suggested in Fig. 2a, the maximum of $|c_p - c_g|$ is smaller than 0.1 M. Thus, σ_{re} is greater than σ_{cl}. It is noteworthy that our model assumes an infinite endothelial cell surface without clefts or pores between endothelial cells. Such assumptions could overestimate c_g, as

Downloaded from www.physiology.org/journal/ajpheart at UCL Library Services (144.082.114.165) on May 14, 2019.

the transport of Na^+ ions to the interstitial fluid side is prevented. Even so, a higher c_g than c_i can still be presumed, as the negative charge of the EGL would prime the accumulation of Na^+ ions. Therefore, the classic Starling principle underestimates the osmotic reflection coefficient of Na^+. We further consider the effect of the varying blood velocities on the evaluation of σ. To distinguish, σ_{im} is used to represent the osmotic reflection coefficient by Eq. (4), and $\sigma_{im} = |\Delta P - FF|/(iRT|c_p - c_g|\gamma) = \sigma_{re}/\gamma$. As γ is usually smaller than 1, a flowing blood would further aggravate the underestimation.

Potential experimental practice

The experimental difficulty resides in the measurement of solute molarity in the subglycocalyx space (c_g), as such a space is extremely difficulty to access. Thus, in a majority of the experimental studies, the osmotic part of the revised Starling principle is simplified. As shown in Eq. (4), the new multiplier, γ, works on the osmotic part, which means experimental measurements with simplification in the osmotic part would be affected by the introduction of γ.

Generally, two principles are used in the measurement of permeability: Landis-Michel's (26) and Li *et al*'s (22). In Landis-Michel's method and its adaptions, the osmotic part is simplified, resulting in the biased measurement results. For example, the aforementioned osmotic reflection coefficient is underestimated. Analogously, the hydraulic conductivity measured by Pocock *et al.*(36) is overestimated. By contrast, Li *et al*'s method refrains from the osmotic term by setting the osmotic pressure to 0. Thus, theoretically, Li *et al*'s experiments would not result in biased estimation of hydraulic conductivity.

Downloaded from www.physiology.org/journal/ajpheart at UCL Library Services (144.082.114.165) on May 14, 2019.

It is noteworthy to recall Betteridge *et al.*'s method in vascular permeability measurement with the aid of advanced imaging techniques (3). The principle is actually consistent with Landis-Michel's (26), and the biased estimation cannot be neglected. However, their method lends an inspiration to access the molarity in the subglycocalyx space by the advanced image technology. If successful, the osmotic term can be precisely measured, and the biased estimation can be eliminated.

Physiological implication.

The physiological role of the EGL includes regulating endothelial permeability by maintaining an oncotic gradient across the endothelial barrier (4). Damages to the EG due to dietary factors or diseases can lead to impairment in the endothelial barrier properties (10, 45). For example, in sepsis, the elevated porosity of endothelium by the inflammatory injury would prime the motion of albumin through the endothelial cleft, which drives oedema (46). Indeed, the present research suggests a way to alleviate oedema by regular moderate exercises: the slightly elevated blood flow velocity after moderate exercise training will result in a reduction in the osmotic part of Eq. (4), leading to a decrease in transvascular fluid permeability which alleviates oedema. The benefit of exercise training to alleviation of oedema was reported in an experimental study (37).

Assumptions of the model.

Some simplifying assumptions are established in the present research. The composition of a realistic EGL is dynamic and continuously affected by the dynamic equilibrium between the soluble components (such as plasma protein) and other blood constituents (39). In this research, a simplified model focused on the EG and Na^+ interactions was constructed, without any plasma proteins. To mimic physiological

Downloaded from www.physiology.org/journal/ajpheart at UCL Library Services (144.082.114.165) on May 14, 2019.

conditions, the molarities of Na^+ and Cl^- in this research are set to be 0.15 M and 0.10 M, respectively, as described previously. These values can be regarded acceptable, as clinic data suggest that the usual reference ranges of serum sodium and chloride of healthy populations are 0.133 M-0.146 M for Na^+ and 0.095 M-0.108 M for Cl^-, respectively. (Clinic data are from Clinical Biochemistry Reference Ranges Handbook by Eastbourne District General Hospital & Conquest Hospital, Hastings, V1.8, ratified in August 2018). Therefore, the physiological implications obtained from the present study are still meaningful.

The simplified model can capture the conformational changes of the EG sugar chains and their interactions with Na^+. However, it fails to predict the impact of other blood constituents on Na^+ transport. In this regard, the 8% deviation in the osmotic permeability is idealized, and can be revised by incorporating additional experimental data. Further wet-lab experiments measuring the permeability under varying flow conditions would contribute to the re-assessment of the Starling principle. Alternatively, retrospective analysis of historical data based on different flow regimes would also benefit the revision of the principle.

The height of the EGL in the present model is of the order of ~10 nm. As mentioned in the introduction, the height of EGL varies within a wide range from 50 to 500 nm. According to the present model, a higher EGL may increase the difficulty in carrying Na^+ out of the EGL layer due to the increased steric hindrance. However, the impact of other blood constituents on Na^+ transport is unknown. Therefore, how the permeability of Na^+ changes with the heights of EGL remains unclear, and additional experimental efforts focusing on the permeability under varying EGL heights are expected to provide further information.

Downloaded from www.physiology.org/journal/ajpheart at UCL Library Services (144.082.114.165) on May 14, 2019.

As mentioned previously, an infinite lipid membrane without clefts or pores between endothelial cells is assumed in this research by the application of period boundary conditions. Hence, transendothelial water flux is not simulated. However, the conclusions obtained from the present research can still be extended to complex situations, as the interactions between sugar chains and ions would not be affected by cleft or pore structures located away from their close proximity.

To conclude, a series of large-scale molecular dynamics simulations were conducted to investigate the microvascular ion transport via the EGL under varying blood flow velocities and different sugar chain configurations. The research leads to new findings about the effects of blood flow velocities and sugar chain configurations on the Na^+ ion transport, and an improved Starling principle. In particular, blood flow promotes the outward Na^+ transport from the near-membrane region to the lumen via the EGL. Furthermore, flow velocity influences the transport via the conformational changes of sugar chains, which affects the Na^+/sugar-chain interactions as well as transferring momentum to ions (see also the schematic of the mechanism in Fig. 6). Detailed analysis on the interactions further reveals that the effects of flow velocity are non-linear. Based on these findings, the widely used Starling principle and its revised version describing the microvascular fluid exchange is further improved by introducing a factor representing the effects of flow velocity and sugar chain configuration. An estimation based on the further revised Starling principle suggests that physiological flow changes the osmotic part of transendothelial water flux by 8% compared with the stationary situation. This research provides a unique insight into ion transport through the EGL by bridging the macroscopic phenomena and atomic events, which adds to our understanding of microvascular fluid exchange.

Downloaded from www.physiology.org/journal/ajpheart at UCL Library Services (144.082.114.165) on May 14, 2019.

It is worth noting that despite significant advances in high-end computing, our MD simulations, though unprecedented, are still confined to simulation time and length of nanoscales, leaving many questions concerning the multiscale multiphysics facets of the EGL unanswered. The links between the dynamics of the EGL and EG-related renal and cardiovascular diseases add a further dimension of complexity that is beyond the scope of this paper. The advent of exascale computing machines, together with the development of reliable coarse-grained MD offers the prospect of an *in silico* technique for investigating EG and cardiovascular problems.

Disclosures

There are no conflicts to declare.

Grants

This work was supported by the UK Engineering and Physical Sciences Research Council under the project UK Consortium on Mesoscale Engineering Sciences (UKCOMES) (Grant Nos. EP/L00030X/1 and EP/R029598/1).

References

1. **Adamson RH, Huxley VH, and Curry FE**. Single capillary permeability to proteins having similar size but different charge. *American Journal of Physiology-Heart and Circulatory Physiology* 254: H304-H312, 1988.
2. **Allen MPA, and Tildesley DJ**. *Computer Simulation of Liquids*. New York: Oxford University Press, 1987.
3. **Betteridge KB, Arkill KP, Neal CR, Harper SJ, Foster RR, Satchell SC, Bates DO, and Salmon AHJ**. Sialic acids regulate microvessel permeability, revealed by novel in vivo studies of endothelial glycocalyx structure and function. *J Physiol* 595: 5015-5035, 2017.
4. **Chelazzi C, Villa G, Mancinelli P, De Gaudio AR, and Adembri C**. Glycocalyx and sepsis-induced alterations in vascular permeability. *Critical care (London, England)* 19: 26-26, 2015.
5. **Cruickshank K, Riste L, Anderson SG, Wright JS, Dunn G, and Gosling RG**. Aortic pulse-wave velocity and its relationship to mortality in diabetes and

Downloaded from www.physiology.org/journal/ajpheart at UCL Library Services (144.082.114.165) on May 14, 2019.

glucose intoleranc: an integrated index of vascular function? *Circulation* 106: 2085-2090, 2002.
6. **Cruz-Chu ER, Malafeev A, Pajarskas T, Pivkin IV, and Koumoutsakos P**. Structure and response to flow of the glycocalyx layer. *Biophys J* 106: 232-243, 2014.
7. **Curry FE, Michel CC, and Mason JC**. Osmotic reflextion coefficients of capillary walls to low molecular weight hydrophilic solutes measured in single perfused capillaries of the frog mesentery. *Journal of Physiology* 261: 319–336, 1976.
8. **Darden T, York D, and Pedersen L**. Particle mesh Ewald: An N·log(N) method for Ewald sums in large systems. *The Journal of Chemical Physics* 98: 10089-10092, 1993.
9. **Eriksson M, Lindhorst TK, and Hartke B**. Differential effects of oligosaccharides on the hydration of simple cations. *J Chem Phys* 128: 105105, 2008.
10. **Eskens BJ, Leurgans TM, Vink H, and Vanteeffelen JW**. Early impairment of skeletal muscle endothelial glycocalyx barrier properties in diet-induced obesity in mice. *Physiological reports* 2: e00194, 2014.
11. **Fu BM, and Shen S**. Structural mechanisms of acute VEGF effect on microvessel permeability. *American Journal of Physiology-Heart and Circulatory Physiology* 284: H2124-H2135, 2003.
12. **Humphrey W, Dalke A, and Schulten K**. VMD: Visual molecular dynamics. *Journal of Molecular Graphics and Modelling* 14: 33-38, 1996.
13. **Huxley VH, Curry FE, Powers MR, and Thipakorn B**. Differential action of plasma and albumin on transcapillary exchange of anionic solute. *American Journal of Physiology-Heart and Circulatory Physiology* 264: H1428-H1437, 1993.
14. **Jiang XZ, Feng M, Luo KH, and Ventikos Y**. Large-scale molecular dynamics simulation of flow under complex structure of endothelial glycocalyx. *Computers & Fluids* 173: 140-146, 2018.
15. **Jiang XZ, Feng M, Ventikos Y, and Luo KH**. Regimes of Flow over Complex Structures of Endothelial Glycocalyx: A Molecular Dynamics Simulation Study. *Scientific Reports* 8: 5732, 2018.
16. **Jiang XZ, Gong H, Luo KH, and Ventikos Y**. Large-scale molecular dynamics simulation of coupled dynamics of flow and glycocalyx: towards understanding atomic events on an endothelial cell surface. *Journal of The Royal Society Interface* 14: 2017.
17. **Jiang XZ, Luo KH, and Ventikos Y**. Reducing Salt Intake and Exercising Regularly: Implications From Molecular Dynamics Simulations of Endothelial Glycocalyx. *Frontiers in Physiology* 9: 2018.
18. **Jorgensen WL, Chandrasekhar J, Madura JD, Impey RW, and Klein ML**. Comparison of simple potential functions for simulating liquid water. *J Chem Phys* 79: 926-935, 1983.
19. **Kim JM, and Baig C**. Precise Analysis of Polymer Rotational Dynamics. *Scientific Reports* 6: 19127, 2016.
20. **Kusche-Vihrog K, Schmitz B, and Brand E**. Salt controls endothelial and vascular phenotype. *Pflugers Archiv : European journal of physiology* 467: 499-512, 2015.
21. **Levick JR, and Michel CC**. Microvascular fluid exchange and the revised Starling principle. *Cardiovasc Res* 87: 198-210, 2010.
22. **Li G, Simon MJ, Cancel LM, Shi ZD, Ji X, Tarbell JM, Morrison B, 3rd, and Fu BM**. Permeability of endothelial and astrocyte cocultures: in vitro blood-brain barrier models for drug delivery studies. *Annals of biomedical engineering* 38: 2499-2511, 2010.

Downloaded from www.physiology.org/journal/ajpheart at UCL Library Services (144.082.114.165) on May 14, 2019.

23. **MacKerell AD, Bashford D, Bellott M, Dunbrack RL, Evanseck JD, Field MJ, Fischer S, Gao J, Guo H, Ha S, Joseph-McCarthy D, Kuchnir L, Kuczera K, Lau FTK, Mattos C, Michnick S, Ngo T, Nguyen DT, Prodhom B, Reiher WE, Roux B, Schlenkrich M, Smith JC, Stote R, Straub J, Watanabe M, Wiorkiewicz-Kuczera J, Yin D, and Karplus M**. All-atom empirical potential for molecular modeling and dynamics studies of proteins. *J Phys Chem B* 102: 3586-3616, 1998.

24. **Marsh JA, and Teichmann SA**. Relative Solvent Accessible Surface Area Predicts Protein Conformational Changes upon Binding. *Structure(London, England:1993)* 19: 859-867, 2011.

25. **Mayes HB, Tian J, Nolte MW, Shanks BH, Beckham GT, Gnanakaran S, and Broadbelt LJ**. Sodium Ion Interactions with Aqueous Glucose: Insights from Quantum Mechanics, Molecular Dynamics, and Experiment. *The Journal of Physical Chemistry B* 118: 1990-2000, 2014.

26. **Michel CC, Mason JC, Curry FE, Tooke JE, and Hunter PJ**. A development of the Landis technique for measuring the filtration coefficient of individual capillaries in the frog mesentery. *Quarterly journal of experimental physiology and cognate medical sciences* 59: 283-309, 1974.

27. **Migliore M, Corongiu G, Clementi E, and Lie GC**. Monte Carlo study of free energy of hydration for Li+, Na+, K+, F−, and Cl− with ab initio potentials. *The Journal of Chemical Physics* 88: 7766-7771, 1988.

28. **Miyamoto S, and Kollman PA**. Settle - an Analytical Version of the Shake and Rattle Algorithm for Rigid Water Models. *J Comput Chem* 13: 952-962, 1992.

29. **Oberleithner H**. Sodium selective erythrocyte glycocalyx and salt sensitivity in man. *Pflugers Archiv : European journal of physiology* 467: 1319-1325, 2015.

30. **Oberleithner H**. Two barriers for sodium in vascular endothelium? *Annals of Medicine* 44: S143-S148, 2012.

31. **Oberleithner H, Peters W, Kusche-Vihrog K, Korte S, Schillers H, Kliche K, and Oberleithner K**. Salt overload damages the glycocalyx sodium barrier of vascular endothelium. *Pflügers Archiv - European Journal of Physiology* 462: 519, 2011.

32. **Paszek MJ, DuFort CC, Rossier O, Bainer R, Mouw JK, Godula K, Hudak JE, Lakins JN, Wijekoon AC, Cassereau L, Rubashkin MG, Magbanua MJ, Thorn KS, Davidson MW, Rugo HS, Park JW, Hammer DA, Giannone G, Bertozzi CR, and Weaver VM**. The cancer glycocalyx mechanically primes integrin-mediated growth and survival. *Nature* 511: 319-325, 2014.

33. **PERL W, and CHINARD FP**. A Convection-Diffusion Model of Indicator Transport through an Organ. *Circulation Research* 22: 273-298, 1968.

34. **Phillips JC, Braun R, Wang W, Gumbart J, Tajkhorshid E, Villa E, Chipot C, Skeel RD, Kale L, and Schulten K**. Scalable molecular dynamics with NAMD. *Journal Computat Chem* 26: 1781-1802, 2005.

35. **Pikoula M, Tessier MB, Woods RJ, and Ventikos Y**. Oligosaccharide model of the vascular endothelial glycocalyx in physiological flow. *Microfluid Nanofluidics* 22: 21, 2018.

36. **Pocock TM, Foster RR, and Bates DO**. Evidence of a role for TRPC channels in VEGF-mediated increased vascular permeability in vivo. *Am J Physiol Heart Circ Physiol* 286: H1015-1026, 2004.

37. **Quilici BCE, Gildo C, Jr., de Godoy JMP, Quilici BS, and Augusto CR**. Comparison of reduction of edema after rest and after muscle exercises in treatment of chronic venous insufficiency. *International archives of medicine* 2: 18-18, 2009.

Downloaded from www.physiology.org/journal/ajpheart at UCL Library Services (144.082.114.165) on May 14, 2019.

38. **Rabelink TJ, and de Zeeuw D**. The glycocalyx--linking albuminuria with renal and cardiovascular disease. *Nature reviews Nephrology* 11: 667-676, 2015.
39. **Reitsma S, Slaaf DW, Vink H, van Zandvoort MAMJ, and oude Egbrink MGA**. The endothelial glycocalyx: composition, functions, and visualization. *Pflügers Archiv - European Journal of Physiology* 454: 345-359, 2007.
40. **Siegel G, Malmsten M, Klüßendorf D, Walter A, Schnalke F, and Kauschmann A**. Blood-flow sensing by anionic biopolymers. *Journal of the Autonomic Nervous System* 57: 207-213, 1996.
41. **Starling EH**. The Arris and Gale Lectures on the Physiological Factors Involved in the Causation of Dropsy .2. The Absorption of Fluids from the Connective-Tissue Spaces - Delivered before the Royal-College-of-Surgeons-of-England, 1896. *Lymphology* 17: 124-129, 1984.
42. **Staverman AJ**. The Theory of Measurement of Osmotic Pressure. *Recl Trav Chim Pay B* 70: 344-352, 1951.
43. **Tarbell JM, and Cancel LM**. The glycocalyx and its significance in human medicine. *J Intern Med* 280: 97-113, 2016.
44. **Tarbell JM, Simon SI, and Curry FRE**. Mechanosensing at the Vascular Interface. *Annu Rev Biomed Eng* 16: 505-532, 2014.
45. **Vlahu CA, Lemkes BA, Struijk DG, Koopman MG, Krediet RT, and Vink H**. Damage of the endothelial glycocalyx in dialysis patients. *Journal of the American Society of Nephrology : JASN* 23: 1900-1908, 2012.
46. **Woodcock TE, and Woodcock TM**. Revised Starling equation and the glycocalyx model of transvascular fluid exchange: an improved paradigm for prescribing intravenous fluid therapy. *British journal of anaesthesia* 108: 384-394, 2012.
47. **Zahr A, Alcaide P, Yang J, Jones A, Gregory M, dela Paz NG, Patel-Hett S, Nevers T, Koirala A, Luscinskas FW, Saint-Geniez M, Ksander B, D'Amore PA, and Argueso P**. Endomucin prevents leukocyte-endothelial cell adhesion and has a critical role under resting and inflammatory conditions. *Nat Commun* 7: 10363, 2016.

Downloaded from www.physiology.org/journal/ajpheart at UCL Library Services (144.082.114.165) on May 14, 2019.

621 **Figure Captions:**

622 **Fig. 1 Initial configuration and charge distributions.** a. Initial configuration of the
623 intact EG system in this research (water and ions are not shown). b. and c. are initial
624 molarity distributions of the sugar chains and ions (Na^+ and Cl^-), respectively
625 (previously published in (16)).

626 **Fig. 2 Distributions of Na^+ molarity differences at changing flow velocities and**
627 **time-evolutions under different situations with varying sugar chain numbers.** a.
628 Distributions of Na^+ molarity differences, $\Delta c = c_g - c_p$, under varying blood velocities
629 resulting from varying external forces (17). Notch values are the mean values. The
630 values in each boxplot were individually obtained from the pertinent experiment
631 conducted for the designated period as shown in Table 1. b. Relative molarity
632 differences in the scenario with shedding sugar chains. Each point was averaged
633 among five consecutive recorded timesteps, and each bar represents the mean ± SD.
634 The first 15-ns results of the N=18 case (Case a in Table 1) were compared with the
635 N=15 (Case e in Table 1) and N=9 cases (Case f in Table 1). c. Distributions of the
636 signs of $\underline{c}$ values in the recorded timesteps in cases with various sugar chain numbers.
637 For the N=18 case, the first 15-ns results were used. In the three cases, signs of 150
638 timesteps were counted. Statistical significances in a and b were checked by ANOVA.
639 ***$p<0.001$ vs. external force of 0; n.s. (not significant) $p>0.05$ vs. external force of 0.

640 **Fig. 3 Coordination numbers of Na^+ and conformations of two sugar chains.** a.
641 Two sugar chains of the same composition with different initial conformations. b.
642 Time-evolution of the coordination numbers of Na^+ around the two sugar chains in
643 one single equilibrium simulation lasting for 8 ns (Case d in Table 1). The
644 coordination numbers are quantified by the numbers of heavy atoms (i.e. nitrogen,
645 oxygen and sulphate atoms) of the sugar chain residues within a cut-off distance of

Downloaded from www.physiology.org/journal/ajpheart at UCL Library Services (144.082.114.165) on May 14, 2019.

2.5 Å around the Na^+ ions. (The value of the cut-off distance is based on the radial distribution result reported in Ref. (9)) c. Probability density distribution for the coordination numbers. The data were collected every 0.1 ns from the 8-ns equilibrium simulation. The probability density distribution was calculated based on the 80 collected statistics. d. Geometric parameters to depict the conformation of a sugar chain. The conformations of sugar chains are measured via a center-to-center vector ($\boldsymbol{R}_{\mathbf{ctc}}$) connecting the two centers of mass of a bisected sugar chain, which is reported effective in describing polymer rotational dynamics (19). e. to g. Time-evolutions of the two sugar chains in terms of the three geometric parameters in the 8-ns equilibrium simulation. The conformations of the two sugar chains vary in dissimilar patterns. Thus, it can be concluded that the sugar chain conformations affect the interactions between the Na^+ ions and sugar chains.

Fig. 4 Probability density distributions of numbers of Na^+ around two segments, and residence rate of Na^+ around both segments. a. Probability density distributions of numbers of Na^+ around two segments with identical residue sequence but different conformations (highlighted yellow in the inner panel). The data were collected every 0.1 ns from the 8-ns equilibrium simulation (Case d in Table 1). The probability density distribution was calculated based on the 80 collected statistics. b. Comparisons of residence rates of Na^+. The higher residence rate of Na^+ in the corner case suggests ions are confined by the corner conformation.

Fig. 5 Flow impact on Na^+ ion transport. a. Average SASA values under varying flow conditions. The lines in the boxes represent the means. Statistical significances were checked by ANOVA. ***p<0.001 vs. external force of 0. b. Average sugar chain conformations and Na^+ velocity fields at first and last timesteps of Case a, projected on a region in the XoZ plane with x from -100 Å to 100 Å and z from 30 Å to 350 Å.

Downloaded from www.physiology.org/journal/ajpheart at UCL Library Services (144.082.114.165) on May 14, 2019.

The sugar chain conformations were averaged over the *y* direction from -40 Å to 40 Å to facilitate visualization. In the calculation of the Na^+ ion velocity fields of individual timestep, the region in the XoZ plane were divided by 20×20 grids, and the velocities of Na^+ ions in each grid were then averaged. c. θ value changes with the external forces. d. Number of Na^+ ions remaining in the sugar-chain-rich region under varying flow situations. In c and d, the probability density distributions were calculated based on data collected every 0.1 ns from individual simulations.

Fig. 6 Schematic of the mechanism for flow impact on Na^+ transport. Flow influences the Na^+ transport via the conformational changes of sugar chains and transferring momentum to Na^+.

Downloaded from www.physiology.org/journal/ajpheart at UCL Library Services (144.082.114.165) on May 14, 2019.

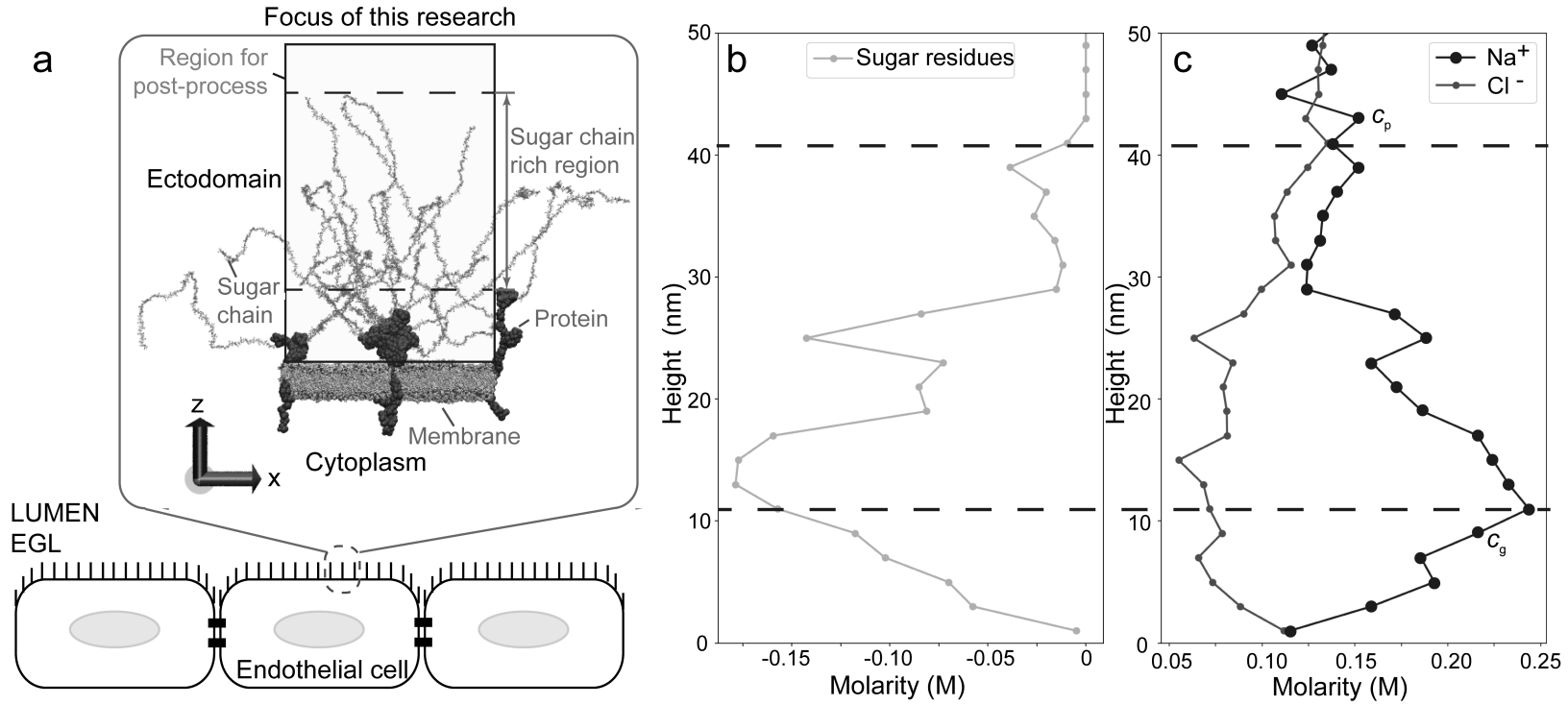

Downloaded from www.physiology.org/journal/ajpheart at UCL Library Services (144.082.114.165) on May 14, 2019.

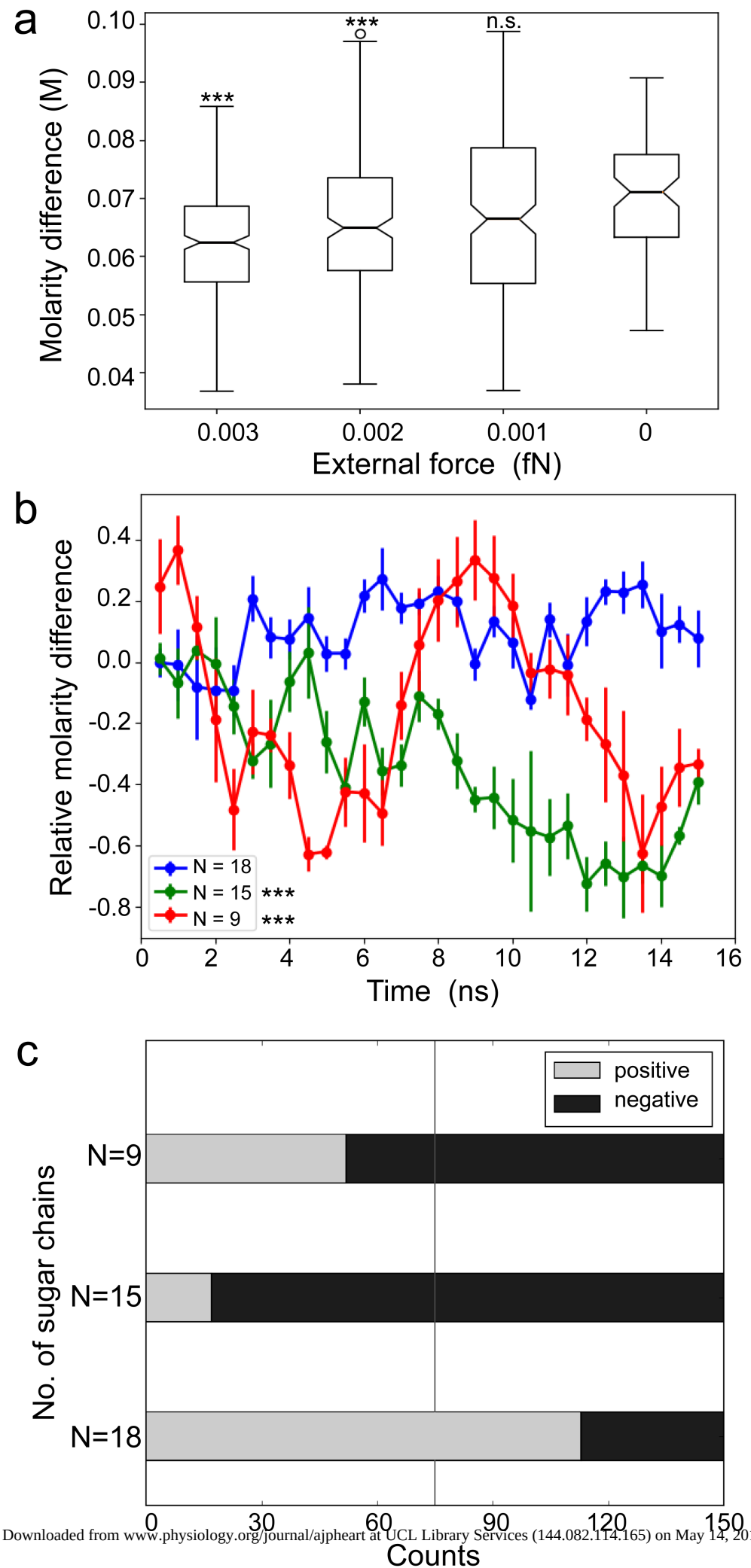

Downloaded from www.physiology.org/journal/ajpheart at UCL Library Services (144.082.114.165) on May 14, 2019.

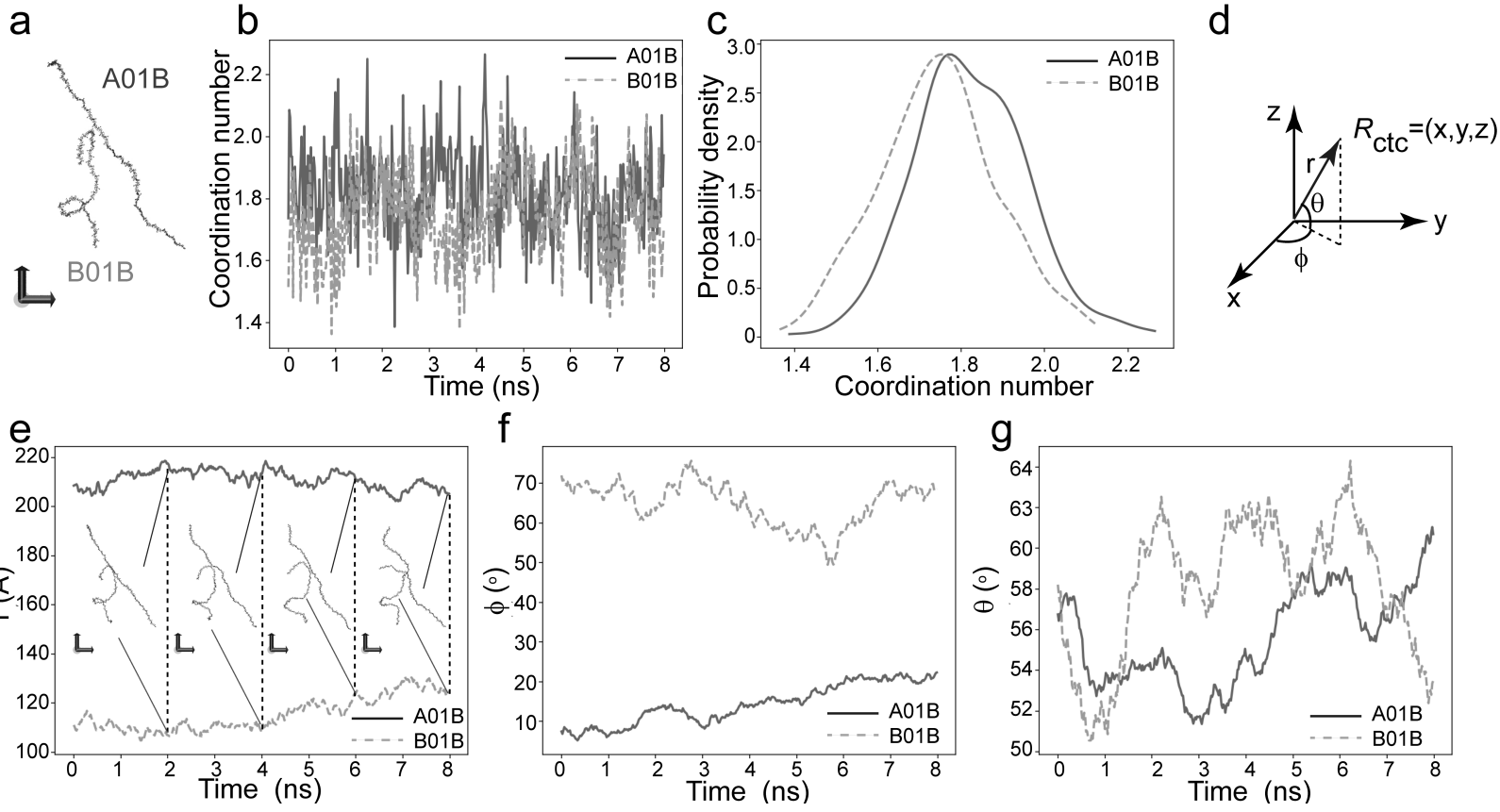

Downloaded from www.physiology.org/journal/ajpheart at UCL Library Services (144.082.114.165) on May 14, 2019.

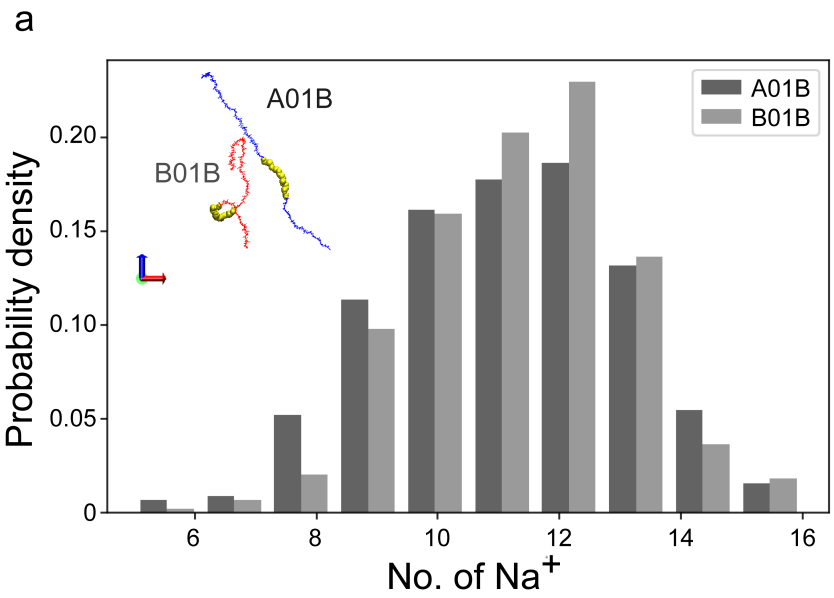

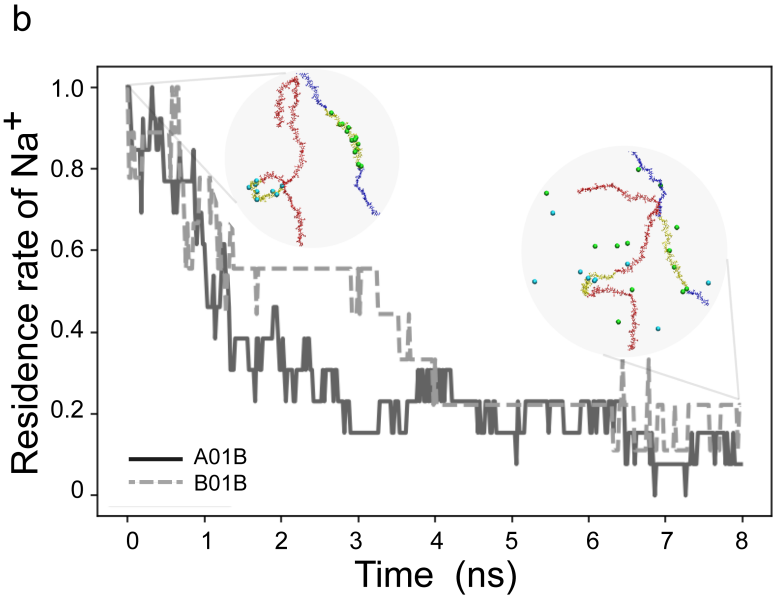

Downloaded from www.physiology.org/journal/ajpheart at UCL Library Services (144.082.114.165) on May 14, 2019.

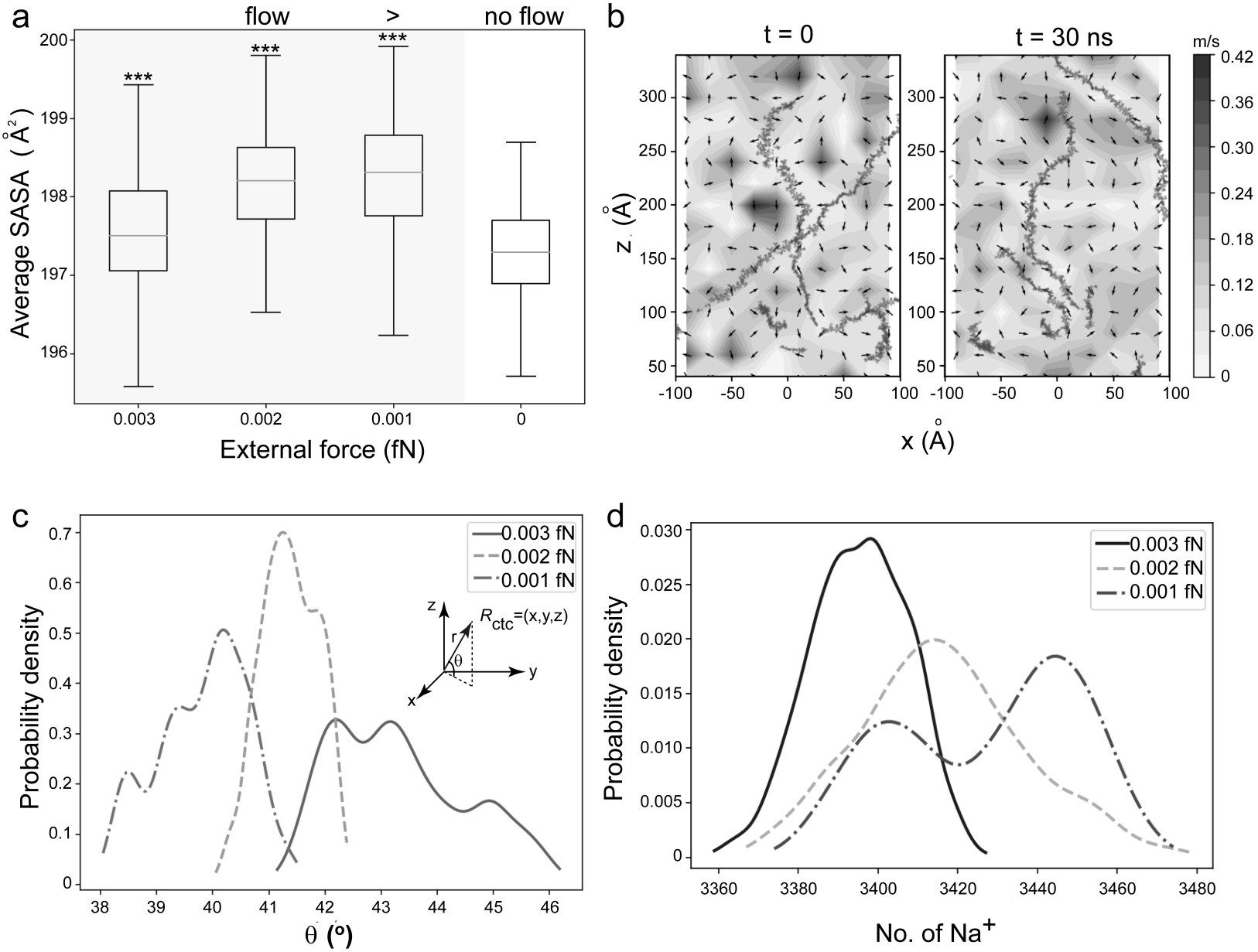

Downloaded from www.physiology.org/journal/ajpheart at UCL Library Services (144.082.114.165) on May 14, 2019.

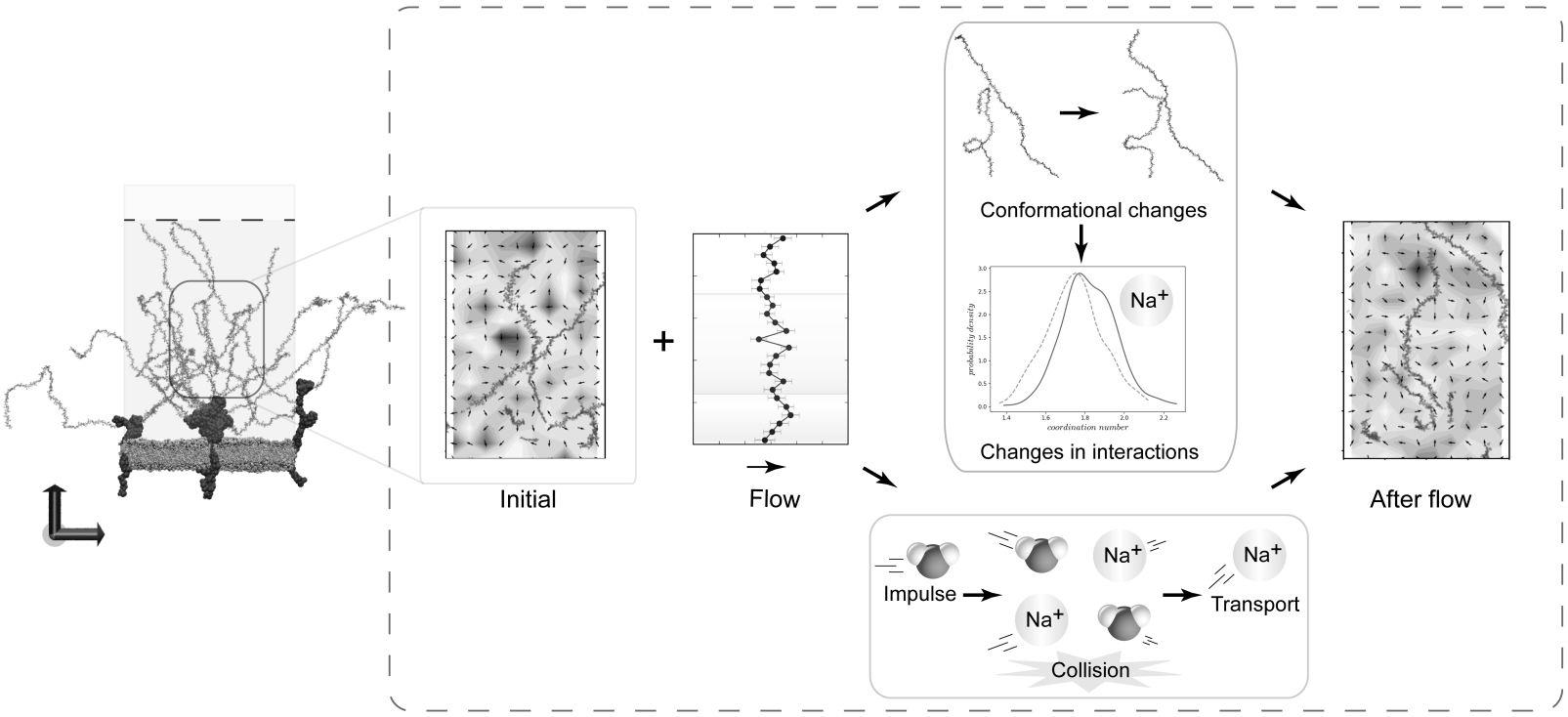

Downloaded from www.physiology.org/journal/ajpheart at UCL Library Services (144.082.114.165) on May 14, 2019.